RSC Mechanochemistry

ROYAL SOCIETY OF CHEMISTRY

PAPER

View Article Online
View Journal

Cite this: DOI: 10.1039/d5mr00030k

Water greatly impacts on the nanomechanical degradation of functionalized surfaces

Martin E. Zoloff Michoff, †* Przemysław Dopieralski ‡ and Dominik Marx

Received 24th February 2025
Accepted 26th January 2026

DOI: 10.1039/d5mr00030k

rsc.li/RSCMechanochem

The functionalization of gold nanoparticles by attaching polyethylene glycol (PEG) chains *via* sulfur-based anchors is a popular approach in technological and nanomedicinal applications. Still, the molecular mechanisms of nanomechanical degradation of such PEGylated gold interfaces exposed to aqueous environments remain unknown. Using isotensional *ab initio* simulations we find that water plays a pivotal role in both purely mechanical rupture and mechanochemical degradation scenarios. These are not determined by force transduction, but rather by distinct interactions of water molecules with the chemical anchors that attach PEG to gold. Based on these insights, shielding against solvation by water is expected to significantly increase their stability toward mechanically-assisted degradation.

Introduction

Functionalization of surfaces by chemical bonding of tailored molecules is a simple and yet powerful way to produce custom-made materials with specific and tunable properties. Biomimetic self-assembled membranes in lithium–sulphur batteries,[1] biocompatible electrodes,[2,3] temperature or strain sensors,[4–6] ultrathin gold films for stretchable electronics,[7] and coated nanocarriers for targeted drug delivery[8–10] are just a few examples of the broad scope of such applications.

The design of these molecules is of utmost importance since they not only protect the material, but also influence its interactions with the surrounding media and, in particular, also affect the material as such through specific hybrid metal–organic interfacial interactions *via* their anchoring junctions.[11–13] Functionalization based on polyethylene glycol (PEG) units, commonly dubbed as "PEGylation", is a broadly used technique to create functionalized and biocompatible surfaces.[11,14,15] Particularly PEGylated gold nanoparticles have been successfully developed to prevent immune response in nanomedicine with enhanced colloidal stability for cancer treatment.[16,17] PEG coatings can be further functionalized in order to bind, for instance, large antibodies to gold nanoparticles as effective biosensors.[18] Such PEG chains are customarily attached to gold species using sulfur (S)-based anchoring groups, such as thiols and the more strongly binding bidentate thioctic (or lipoic) acid group (TA) that offers two instead of only one covalent metal–molecule junction to firmly anchor PEG-TA on gold species.[19–24]

In any real application, the key issue is the stability of the capping layers including their shelf life, as shown for surface-functionalized porous silicon nanoparticles,[25] sulfonated magnetic carbon–cobalt nanoparticles,[26] and perchlorotriphenylmethyl-modified gold surfaces[27] to name but a few. Specifically for PEGylated gold, the relative stability of different mono- *versus* bidentate S-functionalities as anchors has been explored in detail.[28–33] Although most of this work is focused on the structural integrity and thermodynamic stability of Au–S interfaces, there are some experimental[34–37] and theoretical[38–44] studies that address the critical role of their nanomechanical stability. More importantly, also the solvent and notably water has been recently found to greatly influence the stability of such hybrid interfaces.[45,46] This is similar to what has been discovered in the realm of biomechanical processes, where water has been demonstrated to play a crucial role in mechanically activated disulfide bond cleavage.[47–49] Still, the impact of solvent effects on the mechanical stability and chemical degradation mechanisms of metal–organic junctions and interfaces has not yet been addressed, including our own investigations,[40,41,43] and thus remains *terra incognita*. Therefore, we set out to investigate the impact of an aqueous environment at ambient conditions, present in virtually all applications of functionalized metal–organic interfaces, on nanomechanical degradation. Our chosen model, depicted in Fig. 1, consists of a PEG-TA molecule anchored on a gold slab embedded in an explicit water environment. *Ab initio* molecular dynamics (AIMD) simulations[50] were carried out to study, on one side, the purely mechanical degradation process of the hybrid metal–organic interface, and on the other, the mechanochemical reactivity towards the nucleophilic attack of OH^- towards the anchoring S atoms, thus leading to molecular

Lehrstuhl für Theoretische Chemie, Ruhr-Universität Bochum, 44780 Bochum, Germany. E-mail: przemyslaw.dopieralski@chem.uni.wroc.pl

† Permanent address: INFIQC–CONICET, Departamento de Química Teórica y Computacional, Facultad de Ciencias Químicas, Universidad Nacional de Córdoba, Córdoba, Argentina. E-mail: martin.zoloff@theochem.rub.de

‡ Permanent address: Faculty of Chemistry, University of Wroclaw, Joliot-Curie 14, 50-383 Wroclaw, Poland.

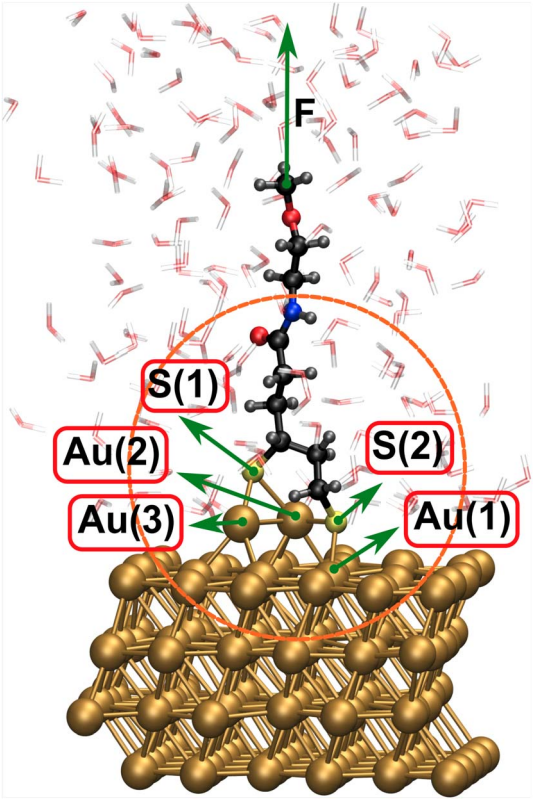

Fig. 1 Computational PEG-TA model, see text, covalently anchored on the Au(111) surface together with all H_2O molecules subject to periodic boundary conditions; note that the initial surface contains an additional Au adatom as detailed in the text while this snapshot visualizes the situation where a second Au atom has already been lifted out of the surface due to pulling the molecule away from the surface as visualized and analyzed in subsequent figures. The relevant Au and S atoms are labeled and the orange circle marks the subsystem highlighted in configurational snapshots depicted in subsequent figures.

detachment from the surface. Most notably, we discover that water plays an overriding role in processes that occur right at stressed metal–organic junctions – thus leading to very different rupture and degradation scenarios from those hitherto known.

Computational details

Preliminary molecular calculations were carried out using the Gaussian program package[51] together with our in-house implementation to add constant external forces in order to explore the stretching response of PEG models with different chain lengths (see Section S-I in the SI for a full account). Once our specific PEG-TA model as analyzed herein has been defined, it was first anchored on a gold surface. Our Au(111) surface model consists of a 5 × 6 slab of 4 gold layers with one additional Au adatom placed at a hollow site, resulting in a total of 121 Au atoms, where the bottom-most layer is kept fixed at the optimized lattice positions throughout. We stress that it has been well established for a long time that gold adatoms are broadly present on reconstructed Au(111) surfaces in experiments and that they play a key role in the Au–S bonding motif; in particular the herringbone-reconstructed (111) surface acts as a source of reactive gold adatoms that drive thiolate self-assembly[52–55] as reviewed in detail.[56–58] The underlying reason is that such adatom defects provide under-coordinated, and thus strongly interacting, reactive anchoring sites for thiolates on reconstructed gold surfaces at typical experimental conditions. In other words, attaching the PEG-TA molecule somewhere on a flat, pristine Au(111) surface would provide an unrealistic model to study nanomechanical degradation processes. Thus, on our gold surface model, the PEG-TA molecule was anchored by means of two S–Au bonds in a tweezer-like arrangement in which the Au adatom is located in between the two S atoms. This particular bonding motif was chosen in such a way as to resemble the S–Au–S pattern exhibited by thiol-based SAMs on Au(111) surfaces at low coverage in the stripe phase[52] and has been optimized in the absence of stretching.

This initial optimized geometry, see Fig. 2a, was subsequently subject to isotensional and isometric pulling procedures (we refer the interested reader to a comprehensive review article on computational covalent mechanochemistry for background and discussion of these different stretching techniques[59]). At this stage, Quantum Espresso software[60] (PWscf) was used for optimizations. The PBE[61] density functional and Vanderbilt's ultrasoft pseudopotentials[62] were employed. This particular electronic structure setup has been carefully validated in previous work[40,43] for very similar hybrid metal–organic interfaces in vacuum. The optimized structures from isotensional stretching of the PEG-TA molecule perpendicular to the surface at constant normal forces of 1.0 and 1.6 nN are shown in Fig. 2b and c, respectively, where a second Au atom gets extracted out of the gold surface in line with earlier work.

As can be seen, applying a constant external force of $F = 1.0$ nN in the direction perpendicular to the Au(111) surface is necessary to fully stretch all soft degrees of freedom. At this stage, a gold atom is also pulled out of the surface. When the external force is increased to 1.6 nN, this Au atom is completely extracted from the surface. Notably, when the force was

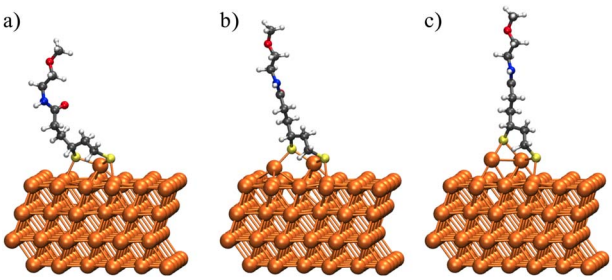

Fig. 2 Isotensional stretching of PEG-TA normal to the Au(111) surface in vacuum. Configuration snapshots of the optimized structures obtained (a) in the absence of external force and by applying a constant external tensile force of (b) $F = 1.0$ and (c) 1.6 nN to the carbon atom in the terminal $-CH_3$ group of the PEG-TA species in the direction perpendicular to the gold slab surface. Note the Au adatom placed at a hollow site in the initial configuration depicted in panel (a) and the second, extracted Au atom in panel (c) as a result of mechanical pulling, see text and the configuration depicted in Fig. 1 subject to full solvation by water molecules.

subsequently decreased to 1.2 nN this structure remained stable, thus representing a stable plastic deformation of the initial bonding pattern due to isotensional stretching. In the early stages of the isometric pulling procedure (refer to Section S-II.A in the SI), a remarkably similar structure, in which a second Au atom is pulled from the surface, is produced (namely structure 2 in Fig. S2). This representative geometry, which will play an important role in nanomechanical detachment scenarios, was then solvated using a total of 144 water molecules, as described in detail in Section S-III of the SI. For these dynamical AIMD simulations[50] at finite temperature that involve the explicit solvent molecules, we have made use of the efficient Car–Parrinello propagation scheme[63] as implemented in the CPMD program package,[64] see Section S-IV. The underlying electronic structure has been computed on-the-fly similarly as in the aforementioned static PWscf calculations, see above for details, using the spin-restricted PBE[61] exchange–correlation functional. The periodic supercell for all AIMD simulations was an orthorhombic box with dimensions of $a = 31.995$ Å, $b = 15.150$ Å, $c = 14.580$ Å that resulted from the initial setup procedure described in detail in the SI. A timestep of 0.0484 fs was used together with Nosé–Hoover thermostating of both nuclei and electrons, with the atomic masses of all hydrogens substituted by deuterium masses to allow for more efficient propagation. For the nuclei, a temperature of 400 K was chosen as it has been shown in the literature to be the value that should be used to describe the structural and dynamical properties of liquid water at ambient conditions in conjunction with the PBE functional.[65]

For the purely mechanical detachment of the PEG-TA from the Au surface subject to explicit solvation by liquid water, we performed AIMD simulations with our in-house modified CPMD code that allows for the inclusion of an arbitrary constant external force, which acted on the carbon atom of the terminal methyl group pointing in the direction perpendicular to the surface, as indicated by the F arrow in Fig. 1. The advantage of this well-established isotensional stretching technique over the usual isometric approach (as reviewed earlier[59]) is the ability of the former to perfectly control the magnitude of the normal tensile force acting on the C-terminus of the PEG-TA chain that is covalently attached to the gold surface. The isotensional approach also provides access to force-transformed free energy surfaces[66] as validated and successfully applied previously.[41,47–49,66] Notably, tensile forces of a few nN as required to break covalent bonds[67] and thus applied in our study are routinely reached in AFM experiments including their operation in isotensional constant force mode.[59,68]

In these constant force AIMD simulations we first performed equilibration runs at a given force value for typically 1–2 ps. We typically observed that the so called "mechanical coordinate (M.C.)", *i.e.* the vertical distance from the fixed Au bottom layer to the terminal carbon, was already stable after such rather short propagation. At this point a snapshot was taken to be the initial configuration for a run in which the external force was increased by an increment of 0.2 nN. This process was repeated starting with a force value of 1.2 nN up to a value of 3.4 nN, at which, as is described in detail below, the complete detachment of TA-PEG from the surface was observed. At each force value, a total of 8–10 ps of AIMD production runs was accumulated in order of have meaningful statistical results. To study the mechanochemical reactivity in alkaline conditions, a water molecule about 3.5 Å away from a given S anchoring atom was selected to be deprotonated and thus become a OH^- species. This nucleophile will covalently attack the PEG-TA/Au(111) junction in aqueous solution in various ways at finite tensile forces to probe the mechanochemical reactivity of the S–Au anchor as analyzed in detail in the "Results and discussion" section. However, a well-known practical limitation of any AIMD simulation is that it cannot access as such the rather long timescales required to observe the breaking and formation of strong covalent bonds since the thermal energy is much smaller than the energy barriers that separate reactants from products. Thus we have employed as usual a well-established enhanced sampling ("rare event") technique in conjunction with dynamical isotensional AIMD simulations.[47,49,59] Specifically, we have used the *ab initio* thermodynamic integration technique based on the so-called "blue moon" sampling[69,70] adapted to the framework of AIMD simulations.[50] The reaction coordinate in all the isotensional AIMD simulations performed in this work has been the distance between the selected sulfur atom, either S(1) or S(2), and the oxygen atom from the attacking nucleophile, *i.e.* OH^-. We note in passing that in the thermodynamic integration approach, alternative reaction pathways were not necessary to be considered since the simulations consistently favored the two primary dissociation routes while not exploring alternative pathways. Moreover, in the case of pure mechanical detachment, also no additional bond breaking events were observed beyond those described.

Finally, a well-acknowledged fundamental issue when dealing with hydroxide ions in aqueous environments, OH^-(aq), is that this ion undergoes Grotthuss-like structural diffusion, thus easily exchanging the particular oxygen atom that hosts the charge defect with others during the reactive AIMD simulations as is well known.[71,72] Hence any reaction coordinate that is based on identifying and constraining the particular oxygen atom of the initial OH^- ion will be unsuccessful in view of structural diffusion of that charge defect since Grotthuss diffusion leads to easy exchange of the specific oxygen atom that is the basis of the hydroxide defect; we note in passing that the very same problem occurs for the hydrated proton in water, H^+(aq). To circumvent this problem we have implemented a well-known algorithm[73] to deal with this situation in an elegant way as proven to be successful in the original work.[73] This algorithm is meant to prevent any proton transfer from any solvent water molecule to the OH^- ion, and thus the structural component to the total diffusion of OH^- is avoided. To this end, whenever the distance between the oxygen of the hydroxide and any hydrogen of any close by H_2O molecule is smaller than 1.3 Å the relative momentum vector of the corresponding pair is reversed in that algorithm.[73]

Results and discussion

As we have anticipated, in this work, we investigate solvent effects on (i) purely mechanical degradation processes as well as on (ii) mechanochemical reactivity of PEGylated gold interfaces toward chemical degradation all fully embedded in liquid water to mimic realistic conditions. All our results, as we discuss in detail below, point to solvation effects as being the key aspect in opening new reaction pathways that were not observed in vacuum in earlier work.[40] These chemical interactions of water molecules with the molecular anchor sites that attach PEG to gold overrule the physical effect of force transduction as we will demonstrate. Thus, solvation is a fundamental aspect that must be considered in any computational work that aims to investigate the nanomechanical stability of gold surfaces at realistic wet-chemical conditions that have been functionalized using sulfur-based anchors, such as PEGylated gold interfaces.

Mechanical degradation of PEG-TA on Au

Let us start with analyzing the purely mechanical detachment process. In the pre-stretched starting configuration, see SI Section S-II, one sulfur atom of the bidentate thioctic acid, S(2), is attached to a single gold atom in the surface, Au(1), while S(1) is connected to two adatoms, Au(2) and Au(3), thus forming a triangular motif, see Fig. 1. The evolution of the hybrid metal–organic junction as a function of F, *i.e.* along the mechanical detachment pathway, consists of a series of elastic deformation regimes highlighted as gray areas in Fig. 3a and b. The change from one elastic regime to the next one occurs *via* sudden plastic deformation events (marked by white regions) which happen in between the maximum and minimum force values, respectively, of the two subsequent elastic regimes. Elastic regimes are consistent with various Au–Au and/or Au–S bonds being continuously stretched to different lengths, whereas plastic transformations are characterized by specific Au–Au and/or Au–S bonds being formed or broken discontinuously as visualized in Fig. 3b together with the configuration snapshots in panel (c). For instance, the plastic deformation observed when the force is increased from 2.0 to 2.2 nN is due to the sudden breaking of the S(1)–Au(2) bond after having reached its maximal elastic elongation of $\approx$2.8 Å resulting in a distance jump to 3.5 Å.

As the force is further increased from 2.4 to 2.6 nN, the interface is modified by the breaking of Au–Au bonds resulting in Au(3) being lifted from the surface. This is even more pronounced upon increasing F to 2.8 nN, with the concurrent breaking of the S(2)–Au(1) bond, setting up the stage for the final detachment. As F increases to 3.2 nN, Au(3) is lifted far away from the surface while the S(1)–Au(3) bond remains strong with the concurrent breaking of the Au(2)–Au(3) bond (upper open green triangle). In addition, also the S(2)–Au(1) bond breaks at this stage leaving Au(1) within the gold surface, which ultimately leads to an upright Au(2)–S(2)–Au(3)–S(1) zig–zag chain pattern that now defines the metal–molecule contact, as illustrated by the configuration corresponding to the still intact junction at 3.2 nN in Fig. 3c, just before detachment occurs. This particular bonding pattern is characteristic of the high force regime, *i.e.* above 3 nN, leading to a highly stressed junction where thermal fluctuations readily induce the final breaking of the gold–PEG anchor, thus leading to the complete detachment of the molecule from the Au surface that yields two different products as depicted in the rightmost snapshots of Fig. 3c.

Most interestingly, two qualitatively different mechanical detachment channels are observed: one in which the rupture of the junction takes place by ripping apart the Au(2)–Au(3) bond as a result of applying sufficient mechanical stress, pathway I. This generates a 6-membered ring-like gold–molecule complex consisting of three C atoms of the thioctic acid (TA) and its two S atoms which bind the Au(3) atom in a tweezer-like ⋯S–Au–S⋯ arrangement after detachment as illustrated in the rightmost lower (F = 3.2 nN) configuration shown in Fig. 3c. In stark contrast, pathway II leads to a chemical isomerization process involving an H atom transfer reaction from a carbon to S(1) that occurs just prior to S(2)–Au(2) and S(2)–Au(3) bond breaking, now leaving all Au atoms attached to the surface as depicted in the rightmost upper (F = 3.4 nN) inset of Fig. 3c. How can these very different mechanical degradation pathways I and II be rationalized? The key turns out to be water. Thermal fluctuations of this liquid can lead to vastly different solvation patterns of the stretched gold–molecule junction as quantified by the analysis of the number of hydrating water molecules; see Section S-VI.A for computational details. In scenario II, one sulfur atom, S(1), is much exposed to solvent molecules which allows for non-covalent interactions (hydrogen bonding) of S(1) with as many as 2.1 water molecules on average, see the upper S(1) histogram for F = 3.4 nN in Fig. 3d. Such significant sulfur–water non-covalent bonding produces a marked weakening of the covalent S(1)–Au(3) bond, which ultimately leads to the detachment of the molecule without any attached Au atom. In stark contrast, the two S atoms are significantly less solvated in scenario I (by only 1.7 and 1.3 water molecules on average, see the full lower S histograms for F = 3.2 nN in Fig. 3d). This reduced solvation number (resulting in reduced non-covalent bonding), in turn, strengthens the covalent S(1)–Au(3) bond, leading to the breaking of the Au(2)–Au(3) bond and the detachment of Au(3) together with the molecule in the tweezer-like complex.

Refined analysis is based on computing the hydration numbers of the two anchoring sulfur atoms S(1) and S(2) due to nearby water molecules; it is computed from counting the number of hydrogen atoms from water molecules within a suitable distance cutoff of 2.9 Å from the respective sulfur atom during the very process of detachment. While at the lower force, F = 3.2 nN, both sulfur atoms have similar hydration numbers before the final detachment of the molecule occurs, it is found that the S(1) sulfur is better solvated after rupture. At the higher force, 3.4 nN, the situation is the opposite: in this case the sulfur atom S(1) is better solvated than S(2) before rupture sets in, while they acquire a quite similar solvation shell after detachment.

This important observation is analyzed and quantified in detail in Fig. 4. It is seen that at F = 3.2 nN, sulfur S(1) is

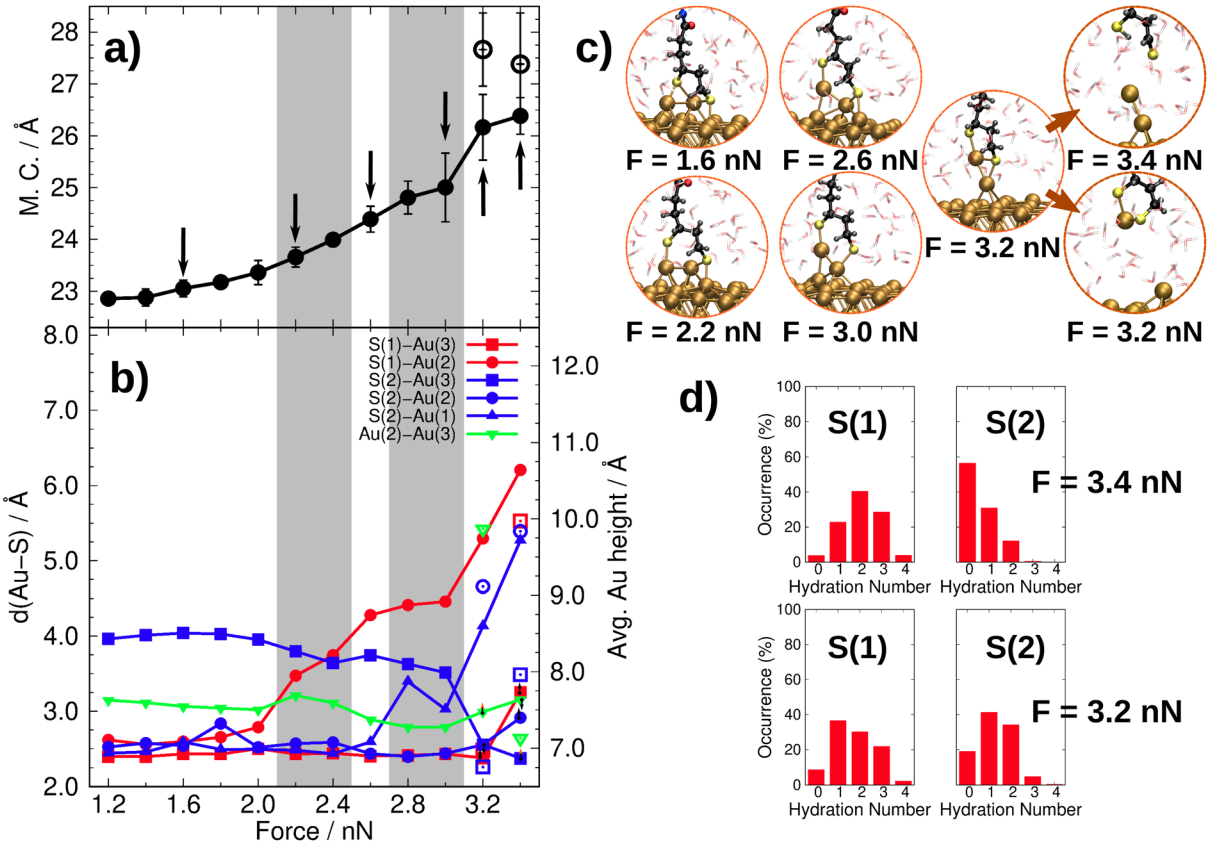

Fig. 3 Panel (a): evolution of the mechanical coordinate (M.C., defined as the distance from the bottom-most Au layer to the terminal C atom) as a measure of stretching the metal–organic junction at the interface as a function of normal tensile force F. The gray areas highlight the different elastic regimes that are separated by plastic deformation events (highlighted using white background) that occur between the respective forces that delimit subsequent elastic regimes (see text). The open symbols at $F = 3.2$ and 3.4 nN refer to the M.C. after full detachment of PEG-TA from Au(111) has occurred with the two respective product configurations depicted on the right side in panel (c). Panel (b): evolution of important S–Au distances (see Fig. 1 for atom labeling) and Au(2)–Au(3) bond distance along the mechanical detachment process as a function of F. The open symbols at $F = 3.2$ and 3.4 nN again refer to the corresponding detachment products. Panel (c): representative configuration snapshots with a focus on the relevant atoms at this metal–organic interface (refer to orange circle in Fig. 1) at relevant force values as indicated by the arrows in panel (a) including the detachment products obtained at $F = 3.2$ and 3.4 nN. Panel (d): hydration number histograms (see Section S-VI.A for computational details) of the two anchoring S atoms at $F = 3.2$ and 3.4 nN right before final detachment, see insets in panel (c) for representative configurations.

similarly solvated before and after the mechanochemical detachment (see two bottom insets in this figure) while S(2) hydration drops down after the detachment and mostly two water molecules are in the first hydration sphere. It should be noted that the histograms displayed here for the hydration of both S atoms in the situation before breakage differ from those shown in Fig. 3d because, in this case, only a very short portion of 3000 sampling steps just before the breaking event was analyzed, whereas in the other case, a much longer AIMD simulation was taken into account to provide averaged information.

Since the hydration number of the sulfur atoms is determined by thermal fluctuations of the local solvation environment and thus by ensemble statistics, it is expected that both pathways are observed upon purely mechanical breaking of the gold–PEG anchor. From previous work of such junctions in vacuum,[40] it is known that mechanical detachment of the TA molecule from gold in the absence of water leads to the tweezer-like ···S–Au–S··· arrangement, which is what we find here only if the S atoms are weakly interacting with water, leading to scenario I. Thus, we discover that mechanical degradation, where no gold atoms are ripped off from the surface together with the detached molecule, provides a novel detachment pathway that is enabled by the presence of solvating water molecules significantly interacting with the anchoring sulfur atoms and, thereby, weakening the respective S–Au bonds. That latter solvation-induced non-covalent sulfur–water interaction effect – with its decisive impact on mechanically stressed and thus weakened covalent sulfur–gold interactions – is obviously not existing in the absence of water, *i.e.* in the gas phase,[40] while it is expected to offer a major mechanical detachment channel that is operational in typical wet lab environmental conditions.

Reactivity of PEG-TA on gold under mechanical stress

Having discovered that water plays a crucial role in purely mechanical degradation processes, we now ask if water also

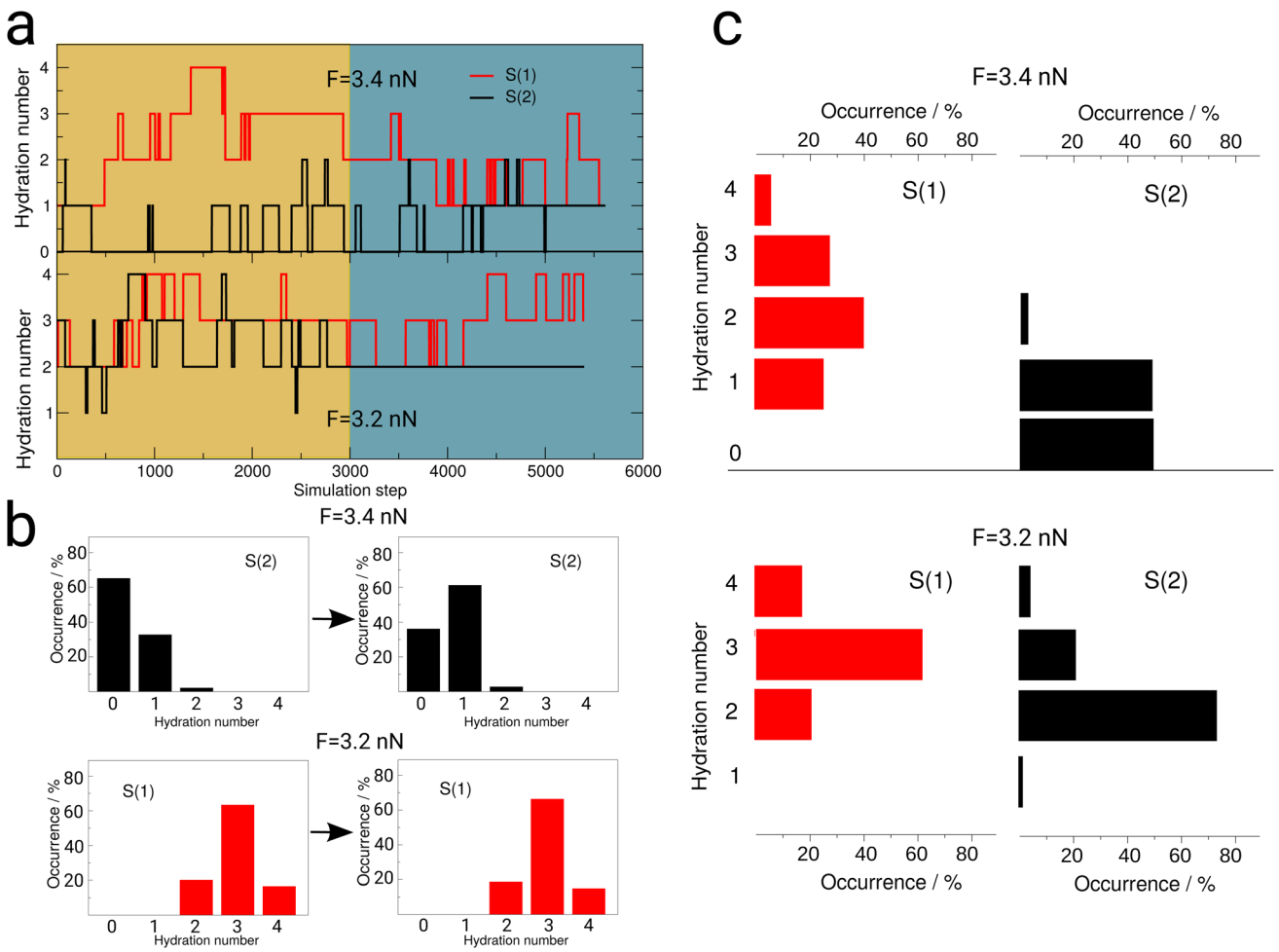

Fig. 4 Statistical analysis of the hydration of the two sulfur atoms by water molecules shortly before and after mechanical detachment at $F = 3.4$ and 3.2 nN (see rightmost panels in Fig. 3c). Panel (a): evolution of the hydration numbers of sulfur atoms S(1) (red line) and S(2) (black line) shortly before (yellow background) and after (blue background) the breaking event, $F = 3.4$ nN (top) and $F = 3.2$ nN (bottom). Panel (b) (top): hydration number histograms of S(2) at $F = 3.4$ nN before (left) and after (right) breaking. Panel (b) (bottom): hydration number histograms of S(1) at $F = 3.2$ nN before (left) and after (right) breaking. Panel (c): hydration number histograms of the two sulfur atoms at the two respective forces $F = 3.4$ nN (top) and $F = 3.2$ nN (bottom) averaged over the full depicted sampling interval before and after detachment.

impacts on the mechanochemical reactivity of PEGylated gold surfaces. Since PEGylation is much used in nanomedicinal applications involving gold-based drugs, we consider the fact that physiological pH is slightly basic,[74,75] implying an excess of solvated hydroxide ions, OH^-(aq). These ions, in turn, are known to attack sulfur sites in aqueous environments (following what is called a nucleophilic reaction mechanism); as usual only a single OH^- ion is included in the AIMD simulation supercell to investigate the very local chemistry that occurs if this nucleophile attacks the sulfur–gold anchor site in alkaline aqueous environments. In total, we studied four different OH^--assisted mechanochemical degradation processes of our fully solvated metal–organic interface as visualized in Fig. 1, namely attack on S(1) and S(2) at constant tensile stresses of $F = 1.2$ and 2.0 nN. These two tensile forces were chosen for two reasons: first of all, they are within the typical range of forces used in single-molecule force spectroscopy experiments to study mechanochemical processes in AFM-type setups.[59,67,68] Secondly, they allow us to disclose the relevant reactive mechanochemical degradation scenarios at representative "lower" and "higher" forces while not simply breaking the junction "by brute force" as already found above in purely mechanical degradation scenarios (recall Fig. 3).

A first surprising finding is that a significant increase in the tensile stress from 1.2 to 2.0 nN does not enhance the reactivity toward mechanochemical degradation: the free energy barriers are found to be very similar at the two forces, compare the dashed to the solid lines in the yellow region of Fig. 5, for the attack on both anchoring atoms S(1) and S(2) distinguished by black and red curves, respectively. This observation is totally different to what is known for the attack by OH^- on mechanically stretched sulfur bonds in biomolecules, where a significant barrier-lowering and, thus, force-dependent chemical activation has been found.[47–49] Interestingly enough, our simulations reveal that one of the sulfurs, namely S(2), is far more susceptible to attack by OH^-, yielding an activation free energy

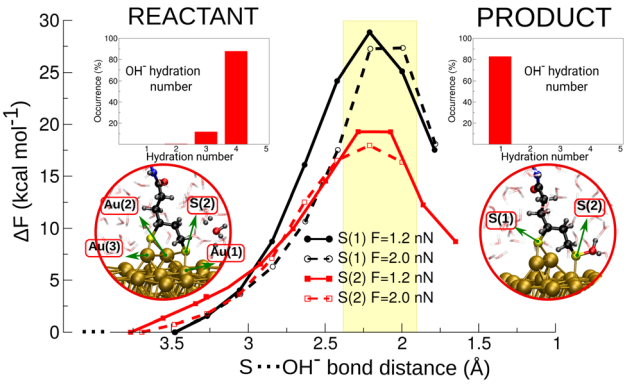

Fig. 5 Mechanochemical reactivity of the S–Au anchor at hybrid metal–organic PEGylated gold interfaces toward chemical degradation subject to explicit solvation in ambient liquid water. Free energy profiles ΔF associated with nucleophilic attack by the OH^-(aq) ion on sulfur atoms S(1) (black lines) and S(2) (red lines) at two constant stretching forces of $F = 1.2$ nN (solid lines) and 2.0 nN (dashed lines) in ambient aqueous solution; the yellow region highlights the transition state regime. The left and right top insets show the hydration number histograms of the oxygen atom of OH^- in the initial (reactant) and final (product) state, respectively, at $F = 1.2$ nN, while the configurations in the bottom insets visualize the reaction site of the respective states for OH^- attacking sulfur S(2), see text.

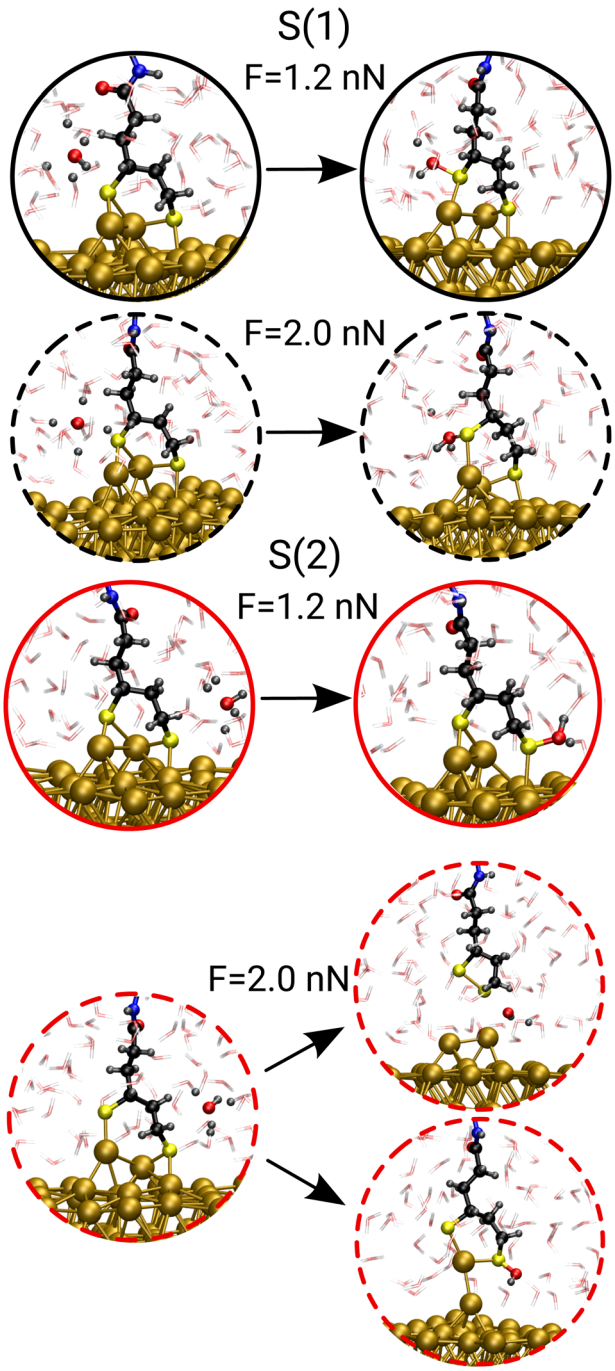

Fig. 6 Overview of all reactants and products at the two forces, $F = 1.2$ and 2.0 nN, for the OH^--assisted reactive mechanochemical degradation processes of our fully solvated metal–organic interface, see text. The attack on the S(1) and S(2) sulfurs at these two constant tensile stresses are shown.

ca. 30% lower with respect to that of S(1), see red *versus* black lines in the yellow region of Fig. 5. Thus, although these two chemical degradation pathways are both essentially force-independent, they differ by as much as $\approx$10 kcal mol^{-1} in activation energy. Considering thermal activation at ambient conditions, *i.e.* $k = A_0 \exp[-\Delta F^{\ddagger}/k_B T]$, this corresponds to a significant acceleration of the degradation rate by many orders of magnitude along the S(2) *versus* the S(1) attack channel. Moreover, although increasing the tensile force from $F = 1.2$ to 2.0 nN does not result in any noteworthy reaction acceleration (compare again solid and broken red lines Fig. 5), the energetically favored S(2) channel leads to different reactions products at both forces, see Fig. 6 for visual analysis based on representative snapshots along the different mechanochemical degradation pathways depending on force and attacked sulfur site. As one can see, while at $F = 1.2$ nN the Au(2)–S(2) bond breaks with the PEG-TA molecule still being attached to the gold surface, two different detachment mechanisms and thus pathways appear at 2.0 nN: one resulting in a 5-membered ring with an intramolecular disulfide bond (with no gold atoms detached from the surface) and another one with a 6-membered ring with one gold atom retrieved from the surface, see the labeled configurations in Fig. 6. In the latter case, the well-known gold adatom mobility on Au(111) surfaces at ambient temperatures generates a situation where one gold atom sticks much out of the surface and, being so exposed, can readily insert into the S(1)···S(2) contact to form two Au–S bonds which leads to the 6-membered ring with its covalent S(1)–Au(3)–S(2) bonding motif, see bottom configuration at $F = 1.2$ nN Fig. 6.

Our observation of pronounced coordination number fluctuations of these exposed gold adatoms is fully consistent with the well-established fluxional character of gold nanoparticles at room temperature.[76] In addition, this fluxionality has been shown to impact the reactivity of gold clusters at the level of reaction pathways and barriers.[77] As a result, different reaction pathways leading to different reaction products can be opened depending on thermal fluctuations as a result of the high mobility in particular of low-coordinated gold atoms at ambient

conditions. This is illustrated with the help of the snapshots and graphs compiled in Fig. 7 whereas we refer the interested reader to SI Section S-VI.B.3 for a comprehensive and detailed analysis. As one can readily see based on Fig. 7, the fluxionality and thus mobility of the low-coordinated gold adatoms right at the stretched (and thus stressed) metal–molecule junction in aqueous solution at room temperature can lead to different mechanochemical degradation pathways and products depicted (top) in terms of snapshot sequences, while comparing the left *versus* right distances and coordination numbers involving the two sulfur atoms and the mechanistically important gold atoms in the bottom graphs provide the detailed correlations along path 1 *versus* path 2, respectively. Of course, full detachment of PEG-TA from the surface eventually takes place in any case, but the gold surface gets destroyed in one scenario by extracting gold atoms together with the molecule, whereas the surface remains intact in the other pathway since only the organic molecule as such gets detached. Incidentally, hydration numbers of OH^- are also found to change considerably, namely from essentially four in the reactant state to a single coordinating water in the product state, which is an enormous change in the hydration pattern. Thus, hydration numbers will be analyzed in detail in what follows.

Having established that mechanochemical degradation based on nucleophilic attack of OH^- on sulfur S(2) in water is greatly favored over S(1), we now try to uncover how this can be understood – finally providing insights into how to control degradation of PEGylated gold surfaces in realistic environments. Guided by the widely accepted idea that optimum force transduction is expected if the attacked bonds are perfectly aligned with the applied tensile force as to maximize their stretching, activation and weakening, we analyze the Au–S–$\vec{F}$

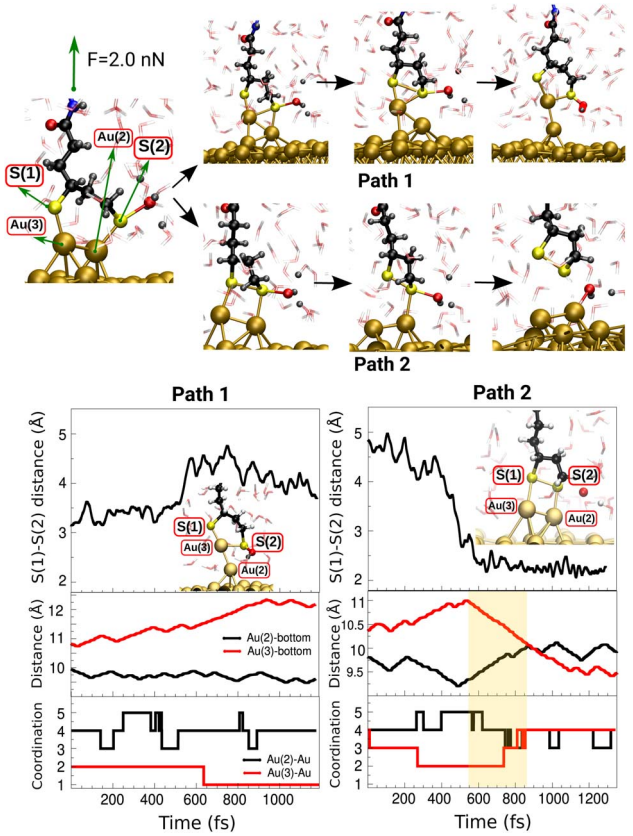

Fig. 7 Analysis of key configurational changes (top panel snapshots) and structural parameters (bottom panel graphs) along the two distinct reactive decomposition pathways 1 and 2, see labeling, observed at a constant stretching force of $F = 2.0$ nN due to nucleophilic attack by OH^-(aq) (highlighted using a red oxygen sphere while the solvation water is transparent), see text. Left bottom panel graphs: analysis of the reactive detachment process leading to formation of the 6-membered ring (with one gold atom detached) and thus no disulfide bond formation along path 1; see the respective top panels for representative configuration snapshots. The upper graph shows the evolution of the S(1)–S(2) distance while the inset visualizes the metal–molecule junction with atom labeling. The middle graph depicts the corresponding evolution of the vertical distance of the two important gold atoms (Au(2) and Au(3)) w.r.t. the fixed bottom layer of gold atoms. The bottom graph provides the concurrent evolution of the coordination numbers of these two gold atoms 2 and 3 with respect to the other gold atoms. Right bottom panel graphs: analysis of the reactive detachment process leading to extraction of the 5-membered disulfide ring (*i.e.* with no gold atoms detached from the surface) along path 2; see the respective top panels for representative configuration snapshots. The properties analyzed in the upper, middle and bottom graphs are the same as for path 1. Note that the *x*-scales provide the AIMD sampling steps in the relevant sampling intervals where the critical events take place along each pathway. The snapshots and graphs of this figure illustrate the discussion of the key findings in the text while their detailed discussion is presented in SI Section S-VI.B.3.

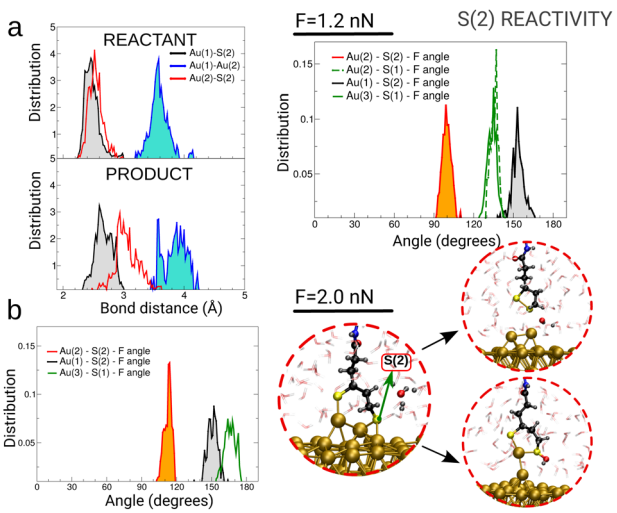

Fig. 8 Analysis of geometrical parameters for nucleophilic attack by the OH^-(aq) ion on sulfur atom S(2) at constant forces. Panel (a): left upper and lower panels depict the bond length distribution functions of Au(1)–S(2) (black line), Au(1)–Au(2) (blue line) and Au(2)–S(2) (red line) in the reactant and product state, respectively, at $F = 1.2$ nN. The right upper panel presents the alignment angle distributions in the reactant state between the Au(1)–S(2) (black line), Au(2)–S(2) (red line), Au(2)–S(1) (broken green line) and Au(3)–S(1) (green line) bonds and the vector of the tensile force ($F = 1.2$ nN) normal to the gold surface. Panel (b): alignment angle of important Au–S bonds with respect to the force vector at $F = 2.0$ nN as in panel (a) (left) and representative snapshots (in the right spheres) of reactant (left) and product (right) states observed during the simulation. See also Fig. 6 and Section S-VI.B for full analysis of all different scenarios discussed in the text.

angle distributions for S(2) reactivity in Fig. 8 at $F = 1.2$ nN and 2.0 nN and for S(1) reactivity in Fig. 9 also at both forces. Surprisingly, the Au(2)–S(2) bond involving the most reactive sulfur atom (orange distributions) features the worst collinear alignment with the tensile direction given by $\vec{F}$ at these two forces, while all other anchoring bonds are much closer to 180°. Thus, taking the alignment with respect to the applied force as an indicator of mechanochemical reactivity, one may conclude that at $F = 1.2$ nN the Au(1)–S(2) bond should be most active, while it should be the other Au(3)–S(1) bond at $F = 2.0$ nN. But unexpectedly, the worst aligned bond breaks orders of magnitude faster, which is counter-intuitive. Even more, the S(1) sulfur atom is the one that is directly attached to the PEG-TA chain along which the stretching force is applied, so that the respective S(1)–Au bond should be more prone to mechanical activation. Thus, we must conclude that the well-known force alignment–reactivity relationship does not provide an understanding of the mechanochemical degradation of PEGylated gold interfaces.

Therefore, as a result of these surprising findings, we consider again the role of water. Indeed, thorough analyses of the accessibility of all four Au–S bonds (as explained in detail in SI Section S-VI.C) reveals that only two of them are spatially accessible by water molecules, and thus prone to attack by OH^- *via* the H-bond network, whereas the other two are fully blocked by atoms of the PEG-TA molecule and thus shielded against attack by this nucleophile, see Table 1. These two water-exposed gold–sulfur bonds are indeed found to be Au(2)–S(1) and Au(2)–S(2). Additionally, stretching of the PEG-TA molecule does not change the shielded nature of the two other bonds, which remain buried independently of tensile stress. Further analyses based on quantifying the solvent-accessible volume of all four bonds unveils that Au(2)–S(2) is the most exposed to the solvent and, therefore, most accessible by OH^- for chemical attack as quantitatively analyzed in Table 1. A closer look at these data provides the explanation why only one of these two bonds is preferred: when analyzing the reaction cone where the Au–S$\cdots X$ distance does not exceed 4.5 Å (see Section S-VI.C for definition), the spatial accessibility of these Au(2)–S(1) and Au(2)–S(2) bonds is drastically different, see their values in Table 1. Based on this comparison, one can immediately see that only in the case of the Au(2)–S(2) bond the reaction cone remains open, thus providing access for nucleophilic attack, while the other bond Au(2)–S(1) is found to be blocked by some other parts of the PEG-TA molecule. In other words: our analysis shows that the most accessible bond, having the largest solvent-accessible volume region open for attack by OH^-, is the Au(2)–S(2) bond. Since that is the bond which features the worst alignment with the force direction, we then find that it is not the efficient transduction of the mechanical force *via* stretching the PEG-TA molecule that determines the rate of mechanochemical degradation of PEGylated gold surfaces, but rather the specific chemistry at the hybrid metal–organic anchor.

Table 1 Spatial accessibility of important gold–sulfur bonds by solvation water, namely Au(3)–S(1), Au(2)–S(1), Au(2)–S(2) and S(2)–Au(1), providing either favorable or unfavorable local environments for nucleophilic attack by OH^- in water based on the solvent-accessible volume region (see SI Section S-VI.C for background and details of this analysis) calculated at two constraint values within the initial (reactant) state (*i.e.* $\xi = S(n)\cdots OH^-$ as reported in the left column) based on the corresponding trajectories from the *ab initio* thermodynamic integration simulations (obtained from isotensional "blue moon" AIMD as explained in SI Section S-V) at constant forces of $F = 1.2$ nN (denoted as @1.2 nN) and $F = 2.0$ nN (@2.0 nN) for both attack pathways, thus involving either sulfur S(1) or S(2). The data are normalized such that 100% (and 0%) denote full accessibility (or full blocking) of the reaction cone as also defined in the SI

	Au(3)–S(1)	Au(2)–S(1)	Au(2)–S(2)	Au(1)–S(2)
S(2)@1.2 nN				
S$\cdots$OH = 3.77 Å	0%	16.1%	68.9%	0%
S$\cdots$OH = 2.92 Å	0%	1.7%	100.0%	0%
S(2)@2.0 nN				
S$\cdots$OH = 3.06 Å	0%	41.1%	68.9%	0%
S$\cdots$OH = 2.85 Å	0%	97.8%	100.0%	0%
S(1)@1.2 nN				
S$\cdots$OH = 3.69 Å	0%	22.6%	73.8%	1.9%
S$\cdots$OH = 2.85 Å	0%	23.1%	66.7%	1.1%
S(1)@2.0 nN				
S$\cdots$OH = 3.48 Å	0%	5.6%	66.0%	0.3%
S$\cdots$OH = 2.85 Å	0%	9.7%	68.4%	8.0%

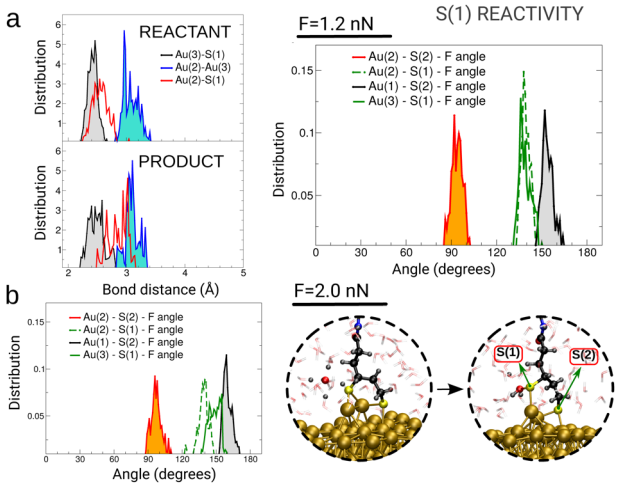

Fig. 9 Analysis of geometrical parameters for nucleophilic attack by the OH^-(aq) ion on sulfur atoms S(1) at constant forces. Panel (a): left upper and lower panels depict the bond length distribution functions of Au(3)–S(1) (black line), Au(2)–Au(3) (blue line) and Au(2)–S(1) (red line) in the reactant and product state, respectively, at $F = 1.2$ nN. The right upper panel presents the alignment angle distributions in the reactant state between the Au(1)–S(2) (black line), Au(2)–S(2) (red line), Au(3)–S(1) (green line) and Au(2)–S(1) (broken green line) bonds and the vector of the tensile force ($F = 1.2$ nN) normal to the gold surface. Panel (b): alignment angle of important Au–S bonds with respect to the force vector at $F = 2.0$ nN as in panel (a) (left) and representative snapshots (in the right spheres) of reactant (left) and product (right) states observed during the simulation. See also Fig. 6 and Section S-VI.B for full analysis of all different scenarios discussed in the text.

Conclusions and outlook

Our extensive *ab initio* simulations of PEGylated gold surfaces in aqueous environments subject to tensile stress reveal a wealth of purely mechanical detachment processes in the first place. Water is found to greatly impact on purely mechanical detachment, leading to degradation of the metal–organic interface where no gold atoms get dissolved. The mechanistic reason is that water molecules can non-covalently interact with the anchoring sulfur atoms (*via* hydrogen bonding), which significantly weakens the covalent gold–sulfur bonds that therefore break more easily, thus leaving all gold atoms on the surface. This scenario is not found at gas phase conditions where gold atoms get detached from the surface, whereas it is highly relevant for purely mechanical degradation of PEGylated gold interfaces in realistic aqueous environments. In addition, their reactive mechanochemical degradation at alkaline pH conditions occurs at a much lower stress due to nucleophilic attack of the sulfur–gold anchor by solvated hydroxide ions, OH^-(aq). In stark contrast to the expectation that the bond best aligned with the external force vector (*i.e.* along the tensile direction) gets most activated and thus breaks most easily – in view of optimal transduction of the applied mechanical force – it is found that water fully governs this scenario as well: it is the most solvent-exposed bond that breaks orders of magnitude faster, the reason being that this local water environment paves the pathway best for nucleophilic attack of sulfur by the solvated OH^-(aq). With regard to applications, our mechanistic insights suggest to chemically shield the anchoring sites of PEGylated gold interfaces against solvation by water in order to significantly increase their stability toward mechanically-assisted degradation processes.

Conflicts of interest

There are no conflicts to declare.

Data availability

All relevant data are included in the article and its supplementary information (SI). Supplementary information is available. See DOI: https://doi.org/10.1039/d5mr00030k.

Acknowledgements

Funded by the Deutsche Forschungsgemeinschaft (DFG, German Research Foundation) under Germany's Excellence Strategy – EXC-2033 – Projektnummer 390677874. MEZM gratefully acknowledges the continuous financial support of SeCyT, Universidad Nacional de Córdoba. PD gratefully acknowledges financial support *via* the National Science Centre of Poland grant no. 2020/37/B/ST4/00423. The computational resources were provided by HLRS (Stuttgart), HPC@ZEMOS, HPC-RESOLV, and BoViLab@RUB.

Notes and references

1 M. Wang, A. E. Emre, J. Y. Kim, Y. Huang, L. Liu, V. Cecen, Y. Huang and N. A. Kotov, *Nat. Commun.*, 2022, **13**, 278.
2 T. Lei, M. Guan, J. Liu, H. C. Lin, R. Pfattner, L. Shaw, A. F. McGuire, T. C. Huang, L. Shao, K. T. Cheng, J. B. Tok and Z. Bao, *Proc. Natl. Acad. Sci. U. S. A.*, 2017, **114**, 5107–5112.
3 C. F. Guo, Q. Liu, G. Wang, Y. Wang, Z. Shi, Z. Suo, C. W. Chu and Z. Ren, *Proc. Natl. Acad. Sci. U. S. A.*, 2015, **112**, 12332–12337.
4 X. Chang, M. Peng, J. Yang, T. Wang, Y. Liu, J. Zheng and X. Li, *RSC Adv.*, 2015, **5**, 75098–75104.
5 S. Zhao, J. Li, D. Cao, G. Zhang, J. Li, K. Li, Y. Yang, W. Wang, Y. Jin, R. Sun and C. P. Wong, *ACS Appl. Mater. Interfaces*, 2017, **9**, 12147–12164.
6 S. Zeng, Z. Yang, Z. Hou, C. Park, M. D. Jones, H. Ding, K. Shen, A. T. Smith, H. X. Jin, B. Wang, H. Jiang and L. Sun, *Proc. Natl. Acad. Sci. U. S. A.*, 2022, **119**, e2118991119.
7 G. Cortelli, L. Patruno, T. Cramer, M. Murgia, B. Fraboni and S. D. Miranda, *ACS Appl. Nano Mater.*, 2021, **4**, 8376–8382.
8 D. Rosenblum, N. Joshi, W. Tao, J. M. Karp and D. Peer, *Nat. Commun.*, 2018, **9**, 1410.
9 P. L. Chariou, O. A. Ortega-Rivera and N. F. Steinmetz, *ACS Nano*, 2020, **14**, 2678–2701.
10 S. S. Liew, X. Qin, J. Zhou, L. Li, W. Huang and S. Q. Yao, *Angew. Chem., Int. Ed.*, 2021, **60**, 2232–2256.
11 K. Ulbrich, K. Hola, V. Subr, A. Bakandritsos, J. Tucek and R. Zboril, *Chem. Rev.*, 2016, **116**, 5338–5431.
12 R. Jin, C. Zeng, M. Zhou and Y. Chen, *Chem. Rev.*, 2016, **116**, 10346–10413.
13 B. Zhang, J. Chen, Y. Cao, O. J. H. Chai and J. Xie, *Small*, 2021, **17**, 2004381.
14 L. Shi, J. Zhang, M. Zhao, S. Tang, X. Cheng, W. Zhang, W. Li, X. Liu, H. Peng and Q. Wang, *Nanoscale*, 2021, **13**, 10748–10764.
15 R. S. Riley, C. H. June, R. Langer and M. J. Mitchell, *Nat. Rev. Drug Discovery*, 2019, **18**, 175–196.
16 D. Van Haute, A. T. Liu and J. M. Berlin, *ACS Nano*, 2018, **12**, 117–127.
17 S. Hočevar, V. Puddinu, L. Haeni, A. Petri-Fink, J. Wagner, M. Alvarez, M. J. D. Clift and C. Bourquin, *ACS Nano*, 2022, **16**, 18119–18132.
18 L.-K. Lin, A. Uzunoglu and L. A. Stanciu, *Small*, 2018, **14**, 1702828.
19 J. Gao, X. Huang, H. Liu, F. Zan and J. Ren, *Langmuir*, 2012, **28**, 4464–4471.
20 E. Oh, K. Susumu, V. Jain, M. Kim and A. Huston, *J. Colloid Interface Sci.*, 2012, **376**, 107–111.
21 G. Liu, Q. Luo, H. Wang, W. Zhuang and Y. Wang, *RSC Adv.*, 2015, **5**, 70109–70116.
22 S. R. Sarker, S. A. Polash, J. Boath, A. E. Kandjani, A. Poddar, C. Dekiwadia, R. Shukla, Y. Sabri and S. K. Bhargava, *ACS Appl. Mater. Interfaces*, 2019, **11**, 13450–13459.
23 T. Y. Hou, F. Y. Shao, Y. T. Sun, K. S. Yang, W. H. Chang and C. A. J. Lin, *Nanoscale*, 2020, **12**, 17786–17794.

24 S. R. Sarker, S. A. Polash, M. N. Karim, T. Saha, C. Dekiwadia, V. Bansal, Y. Sabri, A. E. Kandjani and S. K. Bhargava, *ACS Appl. Bio Mater.*, 2022, **5**, 492–503.
25 R. H. Kang, S. H. Lee, S. Kang, J. Kang, J. K. Hur and D. Kim, *Materials*, 2019, **12**, 580.
26 S. Doswald and W. J. Stark, *Chem.–Eur. J.*, 2021, **27**, 4108–4114.
27 T. Junghoefer, E. M. Nowik-Boltyk, J. A. D. Sousa, E. Giangrisostomi, R. Ovsyannikov, T. Chassé, J. Veciana, M. Mas-Torrent, C. Rovira, N. Crivillers and M. B. Casu, *Chem. Sci.*, 2020, **11**, 9162–9172.
28 B. C. Mei, E. Oh, K. Susumu, D. Farrell, T. J. Mountziaris and H. Mattoussi, *Langmuir*, 2009, **25**, 10604–10611.
29 G. Zhang, Z. Yang, W. Lu, R. Zhang, Q. Huang, M. Tian, L. Li, D. Liang and C. Li, *Biomaterials*, 2009, **30**, 1928–1936.
30 G. Médard and A. C. Papageorgiou, *Nat. Chem.*, 2019, **11**, 20–22.
31 M. H. Stewart, K. Susumu, B. C. Mei, I. L. Medintz, J. B. Delehanty, J. B. Blanco-Canosa, P. E. Dawson and H. Mattoussi, *J. Am. Chem. Soc.*, 2010, **132**, 9804–9813.
32 E. Oh, K. Susumu, R. Goswami and H. Mattoussi, *Langmuir*, 2010, **26**, 7604–7613.
33 E. Wang and Y. Gao, *J. Chem. Phys.*, 2021, **155**, 044302.
34 K. C. Langry, T. V. Ratto, R. E. Rudd and M. W. McElfresh, *Langmuir*, 2005, **21**, 12064–12067.
35 G. Stan, F. W. Delrio, R. I. MacCuspie and R. F. Cook, *J. Phys. Chem. B*, 2012, **116**, 3138–3147.
36 W. Wei, Y. Sun, M. Zhu, X. Liu, P. Sun, F. Wang, Q. Gui, W. Meng, Y. Cao and J. Zhao, *J. Am. Chem. Soc.*, 2015, **137**, 15358–15361.
37 S. Fujii, M. Iwane, S. Furukawa, T. Tada, T. Nishino, M. Saito and M. Kiguchi, *J. Phys. Chem. C*, 2020, **124**, 9261–9268.
38 P. Seema, J. Behler and D. Marx, *Phys. Chem. Chem. Phys.*, 2013, **15**, 16001–16011.
39 H. C. Nguyen, B. M. Szyja and N. L. Doltsinis, *Phys. Rev. B: Condens. Matter Mater. Phys.*, 2014, **90**, 115440.
40 M. E. Zoloff Michoff, J. Ribas-Arino and D. Marx, *Phys. Rev. Lett.*, 2015, **114**, 075501.
41 P. Seema, J. Behler and D. Marx, *Phys. Rev. Lett.*, 2015, **115**, 036102.
42 M. E. Zoloff Michoff, M. E. Castillo and E. P. M. Leiva, *J. Phys. Chem. C*, 2015, **119**, 5090–5097.
43 M. E. Zoloff Michoff, J. Ribas-Arino and D. Marx, *Phys. Rev. Lett.*, 2019, **122**, 086801.
44 S.-Y. Guan, Z.-Y. Cai, J. Liu, R. Pang, D.-Y. Wu, J. Ulstrup and Z.-Q. Tian, *ChemElectroChem*, 2021, **8**, 1123–1133.
45 D. Monego, T. Kister, N. Kirkwood, D. Doblas, P. Mulvaney, T. Kraus and A. Widmer-Cooper, *ACS Nano*, 2020, **14**, 5278–5287.
46 Y. Cao, T. Liu, T. Chen, B. Zhang, D.-e. Jiang and J. Xie, *Nat. Commun.*, 2021, **12**, 3212.
47 P. Dopieralski, J. Ribas-Arino, P. Anjukandi, M. Krupička, J. Kiss and D. Marx, *Nat. Chem.*, 2013, **5**, 685–691.
48 P. Dopieralski, J. Ribas-Arino, P. Anjukandi, M. Krupička and D. Marx, *Angew. Chem., Int. Ed.*, 2015, **55**, 1304–1308.
49 P. Dopieralski, J. Ribas-Arino, P. Anjukandi, M. Krupicka and D. Marx, *Nat. Chem.*, 2017, **9**, 164–170.
50 D. Marx and J. Hutter, *Ab Initio Molecular Dynamics: Basic Theory and Advanced Methods*, Cambridge University Press, Cambridge, 2009.
51 M. J. Frisch, G. W. Trucks, H. B. Schlegel, G. E. Scuseria, M. A. Robb, J. R. Cheeseman, G. Scalmani, V. Barone, B. Mennucci, G. A. Petersson, H. Nakatsuji, M. Caricato, X. Li, H. P. Hratchian, A. F. Izmaylov, J. Bloino, G. Zheng, J. L. Sonnenberg, M. Hada, M. Ehara, K. Toyota, R. Fukuda, J. Hasegawa, M. Ishida, T. Nakajima, Y. Honda, O. Kitao, H. Nakai, T. Vreven, J. A. Montgomery Jr., J. E. Peralta, F. Ogliaro, M. Bearpark, J. J. Heyd, E. Brothers, K. N. Kudin, V. N. Staroverov, R. Kobayashi, J. Normand, K. Raghavachari, A. Rendell, J. C. Burant, S. S. Iyengar, J. Tomasi, M. Cossi, N. Rega, J. M. Millam, M. Klene, J. E. Knox, J. B. Cross, V. Bakken, C. Adamo, J. Jaramillo, R. Gomperts, R. E. Stratmann, O. Yazyev, A. J. Austin, R. Cammi, C. Pomelli, J. W. Ochterski, R. L. Martin, K. Morokuma, V. G. Zakrzewski, G. A. Voth, P. Salvador, J. J. Dannenberg, S. Dapprich, A. D. Daniels, Ö. Farkas, J. B. Foresman, J. V. Ortiz, J. Cioslowski and D. J. Fox, *Gaussian 09, Revision E.01*, Gaussian Inc., Wallingford, CT, 2009.
52 P. Maksymovych, D. C. Sorescu and J. T. Yates, *Phys. Rev. Lett.*, 2006, **97**, 146103.
53 A. Cossaro, R. Mazzarello, R. Rousseau, L. Casalis, A. Verdini, A. Kohlmeyer, L. Floreano, S. Scandolo, A. Morgante, M. L. Klein and G. Scoles, *Science*, 2008, **321**, 943–946.
54 Y. Liu and V. Ozolins, *J. Phys. Chem. C*, 2012, **116**, 4738–4747.
55 D. R. Duijnstee, M. Tromp, W. R. Browne and A. Staykov, *Phys. Chem. Chem. Phys.*, 2025, **27**, 4892–4904.
56 H. Häkkinen, *Nat. Chem.*, 2012, **4**, 443–455.
57 P. Maksymovych, O. Voznyy, D. B. Dougherty, D. C. Sorescu and J. T. Yates, *Prog. Surf. Sci.*, 2010, **85**, 206–240.
58 E. Pensa, E. Cortés, G. Corthey, P. Carro, C. Vericat, M. H. Fonticelli, G. Benítez, A. A. Rubert and R. C. Salvarezza, *Acc. Chem. Res.*, 2012, **45**, 1183–1192.
59 J. Ribas-Arino and D. Marx, *Chem. Rev.*, 2012, **112**, 5412–5487.
60 P. Giannozzi, S. Baroni, N. Bonini, M. Calandra, R. Car, C. Cavazzoni, D. Ceresoli, G. L. Chiarotti, M. Cococcioni, I. Dabo, A. D. Corso, S. de Gironcoli, S. Fabris, G. Fratesi, R. Gebauer, U. Gerstmann, C. Gougoussis, A. Kokalj, M. Lazzeri, L. Martin-Samos, N. Marzari, F. Mauri, R. Mazzarello, S. Paolini, A. Pasquarello, L. Paulatto, C. Sbraccia, S. Scandolo, G. Sclauzero, A. P. Seitsonen, A. Smogunov, P. Umari and R. M. Wentzcovitch, *J. Phys.: Condens. Matter*, 2009, **21**, 395502.
61 J. P. Perdew, K. Burke and M. Ernzerhof, *Phys. Rev. Lett.*, 1996, **77**, 3865–3868.
62 D. Vanderbilt, *Phys. Rev. B: Condens. Matter Mater. Phys.*, 1990, **41**, 7892–7895.
63 R. Car and M. Parrinello, *Phys. Rev. Lett.*, 1985, **55**, 2471–2474.
64 J. Hutter, *et al.*, *CPMD Program Package*, see http://www.cpmd.org.

65 T. A. Pham, T. Ogitsu, E. Y. Lau and E. Schwegler, *J. Chem. Phys.*, 2016, **145**, 154501.
66 P. Dopieralski, J. Ribas-Arino and D. Marx, *Angew. Chem., Int. Ed.*, 2011, **50**, 7105–7108.
67 M. Grandbois, M. Beyer, M. Rief, H. Clausen-Schaumann and H. E. Gaub, *Science*, 1999, **283**, 1727–1730.
68 S. Garcia-Manyes, J. Liang, R. Szoszkiewicz, T. L. Kuo and J. M. Fernandez, *Nat. Chem.*, 2009, **1**, 236–242.
69 E. Carter, G. Ciccotti, J. T. Hynes and R. Kapral, *Chem. Phys. Lett.*, 1989, **156**, 472–477.
70 M. Sprik and G. Ciccotti, *J. Chem. Phys.*, 1998, **109**, 7737–7744.
71 M. E. Tuckerman, D. Marx and M. Parrinello, *Nature*, 2002, **417**, 925–929.
72 D. Marx, A. Chandra and M. E. Tuckerman, *Chem. Rev.*, 2010, **110**, 2174–2216.
73 J. Blumberger, B. Ensing and M. L. Klein, *Angew. Chem.*, 2006, **118**, 2959–2963.
74 S. Düwel, C. Hundshammer, M. Gersch, B. Feuerecker, K. Steiger, A. Buck, A. Walch, A. Haase, S. J. Glaser, A. Schwaiger and F. Schilling, *Nat. Commun.*, 2017, **8**, 15126.
75 M. Tanriver, Y. C. Dzeng, S. D. Ros, E. Lam and J. W. Bode, *J. Am. Chem. Soc.*, 2021, **143**, 17557–17565.
76 A. Vargas, G. Santarossa, M. Iannuzzi and A. Baiker, *Phys. Rev. B: Condens. Matter Mater. Phys.*, 2009, **80**, 195421.
77 M. Gao, A. Lyalin, M. Takagi, S. Maeda and T. Taketsugu, *J. Phys. Chem. C*, 2015, **119**, 11120–11130.